

NUMERICAL INVESTIGATION OF THE NANOFLUID NATURAL CONVECTION FLOW IN A CPU HEAT SINK USING BUONGIORNO TOW-PHASE MODEL

Yamina Anouar ^{1*} and Abderrahim Mokhefi ²

¹ Department of Hydraulics, University of Science and Technology of Oran – Mohammed Boudiaf, B.O. Box 1505, El-M'Naouer, 31000, Oran, Algeria
e-mail: yaminaa833@gmail.com

² Mechanics, Modeling and Experimentation Laboratory L2ME, Faculty of Technology, Bechar University B.P.417, 08000, Bechar, Algeria
e-mail: abderahimmokhefi@yahoo.fr

**corresponding author*

Abstract

In this paper, a numerical investigation using the finite element method on the cooling capacity of an electronic heat sink has been presented. This heat sink is intended for cooling applications of micro-computer CPUs. It deals with a parallelepipedal block with rectangular fins, filled with a nanofluid and crossed by four cylindrical pipes in which a cooling gas flows and dissipates the heat generated by the processor. Indeed, the cooling occurs by three transfers: the first one evacuates the heat from the processor towards the gas, the second one transfers this heat towards the nanofluid and the last one is cooled from the ambient air by means of the fins laterally arranged on the block. From this work, it has been planned to contribute to the study of the behavior of a nanofluid in the heat sink in the presence of a uniform magnetic field in order to enhance the operating and cooling performances. The effects of some control parameters have been highlighted on the hydrodynamic, thermal, and mass behavior of the nanofluid, namely: the Rayleigh number ($10^3 \leq Ra \leq 10^5$), the Hartmann number ($0 \leq Ha \leq 100$), the angle of inclination of the magnetic field ($0 \leq \gamma \leq 90^\circ$) and the nanoparticles diameter ($1 \text{ nm} \leq dp \leq 10 \text{ nm}$). On the other hand, a new fin design has been proposed in this study allowing the enhancement of the heat exchange rate with ambient medium. The studied phenomenon is governed by the equations of the two-phase nanofluid model proposed by Buongiorno and which describe the following balances: mass, momentum, energy and nanoparticles. The system of partial differential equations with initial-boundary conditions has been solved by the finite element method. After performing a mesh independence check and validating with previous papers, the results of the investigation were presented. They showed that the application of a magnetic field significantly reduces the rate of heat exchange. However, increasing the angle of inclination of this field promotes convective heat transfer. Moreover, the use of zigzag fins improves the cooling rate by about 4% for amplitude of 0.05 compared to the standard configuration.

Keywords: Buongiorno, Heat transfer, nanofluid, nanofluid, natural convection

1. Introduction

Thermal transfer is one of the prevailing physical phenomena in all technological and industrial applications. It is also considered as one of the factors that determine the performance of the thermal system (Spizzichino et al. 2020; Wu et al. 2020; Basu et al. 2008; Mokeddem et al. 2019; Ibrahim et al. 2019). Among the most important of these thermal phenomena is what is known as the cooling technique, which is based mainly on the use of the static or moving fluid around a solid and hot body with the intention of transferring that thermal energy from the hot body towards the fluid (Laidoudi et al. 2017; Rejeb et al. 2022; Hassen et al. 2013; Laidoudi et al. 2021a; Selimefendigil et al. 2018). This type of study can be used to develop high-performance thermal exchangers, accelerate the cooling process in electronic systems, works related to medical products, solar collectors and other applications.

Through the previous papers, it was realized that thermal activity has a clear relationship with the quality of fluid, the shape of the body and its temperature, in addition to the external factors such as the presence of relative forces. For example, Darzi et al. (2017) conducted an in-depth study on the positioning of two hot bodies inside a square room with the effect of thermal buoyancy. Also, the upper wall of the room moves from left to right in an ordinary and steady manner. The purpose of this research is to develop the thermal regime of hot bodies by determining the position that allows the raise of thermal activity. Mishra et al. (2017) presented a paper on the rheological effects of the fluid on heated bodies trapped in a chamber with two openings for the entry and exit of the fluid. This work was done without the influence of any external force and by not applying the effect of thermal buoyancy. The work mainly focused on clarifying the behavior of the rheological properties of the fluid and the positioning of the bodies on the thermal activity. Karimi et al. (2016) focused on presenting a study aimed at determining the effect of body size on thermal activity. This research was conducted inside a chamber with two equal and opposite openings. Thermal activity occurs under the influence of thermal buoyancy factor. Chatterjee et al. (2014) conducted an investigation in which they combined the effect of factors on the thermal activity of a system consisting essentially of two hot bodies enclosed in a closed chamber with cold walls. The two bodies also rotate at a constant speed. Also, there is an effect of the applied magnetic field at a fixed angle. The results show how the magnetic field affects the thermal behavior of the system. Talkhonchek et al. (2016) included the impact of time on thermal activity of hot bodies inside a ventilated room. The results showed that there is an effect of time when the velocity of the fluid entering the chamber is very high. This effect was manifested in the presence of changes in thermal activity in terms of time for a constant velocity. Park et al. (2012) presented an investigation showing the relationship between the placement/size of hot bodies and heat transfer in a closed room without the impact of magnetic. The fluid is moving here as a result of thermal buoyancy. Chatterjee et al. (2017) also presented a very important paper where they combined the effect of rotating hot bodies with the magnetic field inside a closed room. A strong evolution of thermal activity in terms of rotational speed was understood. Laidoudi et al. (2021b) studied the thermal activity between two thermally different objects locked inside an isolated room. The aim of the study was to evaluate the thermal activity between the two elements under a set of conditions. The work was done without the inclusion of the Lorentz force, but with the effect of thermal buoyancy.

Recently, a significant number of studies have appeared that study the thermal activity and the element affecting it for hot bodies trapped in closed room. Among these researches, there is a tendency to study the geometrical form of the system (El-Shorbagy et al. 2021; Mostafa et al. 2011; Ghasemi et al. 2020; Selimefendigil et al. 2015; Selimefendigil et al. 2020; Laidoudi et al. 2021c; Yang et al. 2020). There are those who mainly care about the geometric shape of the trapped bodies, such as Zeitoun et al. 2011; Laidoudi et al. 2020a; Rashidi et al. 2013; Laidoudi et al. 2022a; and Mourad et al. 2021. While others cared about the shape of the chamber (Tayebi

et al. 2021; Farahani et al. 2022; Aliouane et al. 2021; Aissa et al. 2022a; Aissa et al. 2022b). In the end, an important rule was understood, which is that the geometry of the thermal system has an important role in heat transfer, and it must be studied in each case according to the proposed system. On other hand, some researchers studied the fluid quality and its effect on the thermal evolution of the system. Some of them used non-Newtonian fluids (Guendouci et al. 2021; Laidoudi et al. 2022b; Yigit et al. 2017; Laidoudi et al. 2020b; Matin et al. 2013; Ramla et al. 2022), while others exploited nanofluids in order to augment the thermal comportment (Garooosi et al. 2014; Sheikholeslami et al. 2015; Maneengam et al. 2022; Laidoudi et al. 2022c). In the end, it was understood that the type of fluid and its behavior relatively affect the thermal activity, and that this effect varies from one thermal system to another.

Through our treatment of this subject, it turns out that the use of nanofluids plays an important role in strengthening thermal activity, especially if the studied system is applied to a magnetic field. Most of the studies did not take into account the effect of nanoparticle size on the thermal activity and fluid dynamic pattern. So, we conducted this work to reinforce the findings around this idea. This paper combines the geometrical effects of the system and fluid quality on thermal transfer of heated bodies inside a closed room. The issues addressed here are: the magnetic field strength and angle of application, thermal buoyancy intensity and nanoparticle size in addition to its density.

2. Geometrical presentation

The cooling system CPU presented in the present paper is one of the hydraulic heat sinks type using the latest technology in thermal applications (Alsarraf et al. 2020). This technology uses a special type of heat transfer fluid called nanofluid. The heat sink is installed on a central processing unit CPU where several pipes and fins are installed to enhance the cooling efficiency. In addition, there is an empty space between the fins and the pipes where a nanofluid is filled to increase the efficiency of the cooling system (Fig. 1). Due to the symmetry of the problem, the studied geometry is reduced to a two-dimensional square cavity of length H filled with alumina/water nanofluid as shown in Fig. 2. The right and left walls are maintained at a cold temperature (T_c) according to the fins effect. However, the top and bottom walls are considered adiabatic. Moreover, four pipes of circular cross section, of diameter D , symmetrical to the center of the cavity and speared with a distance L are introduced in the middle of the cavity where each one is maintained at a hot temperature T_h . Furthermore, a uniform magnetic field is applied to the cavity with an intensity of B_0 as shown in Fig. 2.

The present investigation consists of analyzing the heat transfer performances of this type of heat sinks by considering the effects of Brownian motion and thermophoretic diffusion that occur due to the presence of nanoparticles suspended in the pure water used. The analysis is based on the effect of the nanoparticles migration on the cooling rate within the cooling dispositive. On the other hand, the effect of the magnetic field intensity and its direction on the cooling rate of this type of electronic component is also analyzed.

We also present a geometric analysis of the effect of installing zigzag fins on the cooling capacity within the presented heat sink. Indeed, as in most of the cases, the corrugation extension of the walls of the heating or cooling surfaces increases. The new shape proposed in our paper is shown in Fig. 3.

The thermo-physical proprieties of the nanofluid are considered constant. They are shown in Table 1.

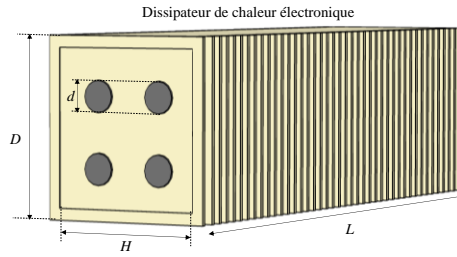


Fig. 1. 3D reduced geometry.

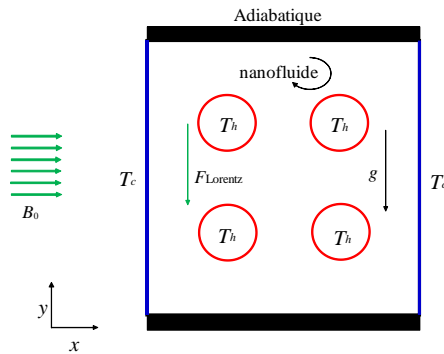


Fig. 2. 2D heat sink section.

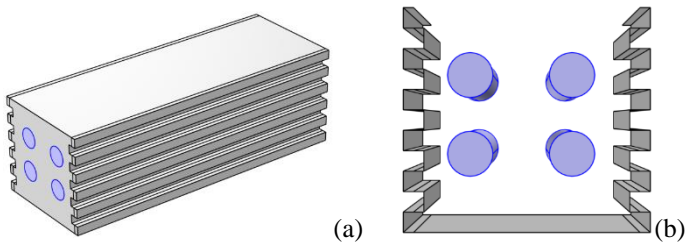


Fig. 3. Form of heat sink proposed in our study. (a) Block with zigzagged fins. (b) Zigzag shape.

Physical properties	Density [kg/m ³]	Dynamic viscosity [Pa.s]	Thermal conductivity [W/(m.K)]	Specific heat [J/(kg.K)]	Electrical conductivity [S/m]	Thermal expansion [1/K]
water	997.1	0.001	0.613	4179	0.050	21.0×10^{-5}
Al ₂ O ₃	3970	-	40.00	765.0	1×10^{-10}	0.85×10^{-5}

Table 1. Physical properties of the base fluid and the nanoparticles.

3. Governing equations

3.1. Dimensional governing equations

On the two-dimensional domain schematized in Fig. 2, the equations that govern the magnetohydrodynamic natural convection are represented. Due to the study of the impact of the alumina nanoparticles migration on the heat transfer, the two-phase flow Buongiorno model is employed. Thus, the equations that express the mass conservation, momentum (Navier-Stokes), energy, and nanoparticles migration are used to model the heat transfer within the heat sink. In fact, the two-phase Buongiorno model is used to study the effects of Brownian motion and thermophoresis of nanoparticles on the flow intensity, the heat transfer and the mass transfer. In this model, the spatio-temporal distribution of nanoparticle concentrations within the base fluid is considered non-homogeneous. This model focuses on a full coupling between the mathematical equations governing the study, by introducing very specific boundary conditions that express the displacement of nanoparticles under the effect of thermo-mass gradients. In order to simplify the study, it has been taken into account that:

- The fluid is considered as a homogeneous and isotropic medium.
- The flow in the cavity is laminar incompressible. This is obtained by reducing the buoyancy force.
- The physical parameters of the Newtonian nanofluid with Al₂O₃ nanoparticles, have been introduced in the differential system through the correlations of the nanometric suspension quoted in the literature.
- Radiation, work under pressure and viscous dissipations are all neglected in this study.
- The physical properties of the base fluid as well as the nanoparticles are all considered constant, with the exception of the density of the base fluid which, by its change as a function of temperature creates a force called buoyancy. This force is introduced in the vertical direction through the Boussinesq approximation.

Mass equation

$$\frac{\partial u}{\partial x} + \frac{\partial v}{\partial y} = 0 \quad (1)$$

Momentum equations

$$\rho_{nf} \left(\frac{\partial u}{\partial t} + u \frac{\partial u}{\partial x} + v \frac{\partial u}{\partial y} \right) = -\frac{\partial p}{\partial x} + \mu_{nf} \left(\frac{\partial^2 u}{\partial x^2} + \frac{\partial^2 u}{\partial y^2} \right) + \sigma_{nf} B_0^2 (v \cos \gamma \sin \gamma - u \sin \gamma) \quad (2)$$

$$\begin{aligned} \rho_{nf} \left(\frac{\partial v}{\partial t} + u \frac{\partial v}{\partial x} + v \frac{\partial v}{\partial y} \right) &= -\frac{\partial p}{\partial y} + \mu_{nf} \left(\frac{\partial^2 v}{\partial x^2} + \frac{\partial^2 v}{\partial y^2} \right) + \\ &+ \sigma_{nf} B_0^2 (u \cos \gamma \sin \gamma - v \cos \gamma) + \rho_{nf} g \beta_{nf} (T - T_c) \end{aligned} \quad (3)$$

Energy equation

$$\begin{aligned} \frac{\partial T}{\partial t} + u \frac{\partial T}{\partial x} + v \frac{\partial T}{\partial y} = \alpha_{nf} \left(\frac{\partial^2 T}{\partial x^2} + \frac{\partial^2 T}{\partial y^2} \right) + D_B \left(\frac{\partial T}{\partial x} \frac{\partial \phi}{\partial x} + \frac{\partial T}{\partial y} \frac{\partial \phi}{\partial y} \right) + \\ \frac{D_T}{T_c} \left[\left(\frac{\partial T}{\partial x} \right)^2 + \left(\frac{\partial T}{\partial y} \right)^2 \right] \end{aligned} \quad (4)$$

Nanoparticles equation

$$\frac{\partial \phi}{\partial t} + u \frac{\partial \phi}{\partial x} + v \frac{\partial \phi}{\partial y} = D_B \left(\frac{\partial^2 \phi}{\partial x^2} + \frac{\partial^2 \phi}{\partial y^2} \right) + \frac{D_T}{T_c} \left(\frac{\partial^2 T}{\partial x^2} + \frac{\partial^2 T}{\partial y^2} \right) \quad (5)$$

3.2. Dimensionless governing equations

In order to make the studied problem more general, a set of dimensionless variables has been introduced in equations Eqs. (1)-(5) as follows:

$$X = \frac{x}{H}, Y = \frac{y}{H}, U = \frac{uH}{\alpha_{nf}}, V = \frac{vH}{\alpha_{nf}}, P = \frac{pH^2}{\rho_{nf} \alpha_{nf}^2}, \theta = \frac{T - T_c}{T_h - T_c}, \phi = \frac{\phi}{\phi_0} \quad (6)$$

After substituting the formula Eq. (6) in the balances Eqs. (1)-(5), they become:

Dimensionless Mass equation

$$\frac{\partial U}{\partial X} + \frac{\partial V}{\partial Y} = 0 \quad (7)$$

$$\begin{aligned} \frac{\partial U}{\partial \tau} + U \frac{\partial U}{\partial X} + V \frac{\partial U}{\partial Y} = - \frac{\partial P}{\partial X} + \frac{\nu_{nf}}{\nu_f} \frac{\alpha_f}{\alpha_{nf}} \text{Pr} \left(\frac{\partial^2 U}{\partial X^2} + \frac{\partial^2 U}{\partial Y^2} \right) + \\ \frac{\rho_f}{\rho_{nf}} \frac{\sigma_{nf}}{\sigma_f} \text{Pr Ha}^2 (V \cos \gamma \sin \gamma - U \sin \gamma) \end{aligned} \quad (8)$$

$$\begin{aligned} \frac{\partial V}{\partial \tau} + U \frac{\partial V}{\partial X} + V \frac{\partial V}{\partial Y} = - \frac{\partial P}{\partial Y} + \frac{\nu_{nf}}{\nu_f} \frac{\alpha_f}{\alpha_{nf}} \text{Pr} \left(\frac{\partial^2 V}{\partial X^2} + \frac{\partial^2 V}{\partial Y^2} \right) + \\ \frac{\rho_f}{\rho_{nf}} \frac{\sigma_{nf}}{\sigma_f} \text{Pr Ha}^2 (U \cos \gamma \sin \gamma - V \cos \gamma) + \frac{\beta_{nf}}{\beta_f} \text{Ra Pr } \theta \end{aligned} \quad (9)$$

$$\begin{aligned} \frac{\partial \theta}{\partial \tau} + U \frac{\partial \theta}{\partial X} + V \frac{\partial \theta}{\partial Y} = \frac{\partial^2 \theta}{\partial X^2} + \frac{\partial^2 \theta}{\partial Y^2} + \frac{k_f}{k_{nf}} \text{N}_B \left(\frac{\partial \theta}{\partial X} \frac{\partial \phi}{\partial X} + \frac{\partial \theta}{\partial Y} \frac{\partial \phi}{\partial Y} \right) + \\ \frac{k_f}{k_{nf}} \text{N}_T \left[\left(\frac{\partial \theta}{\partial X} \right)^2 + \left(\frac{\partial \theta}{\partial Y} \right)^2 \right] \end{aligned} \quad (10)$$

$$\frac{\partial \phi}{\partial \tau} + U \frac{\partial \phi}{\partial X} + V \frac{\partial \phi}{\partial Y} = \frac{\alpha_{nf}}{\alpha_f} \frac{1}{\text{Le}} \left[\left(\frac{\partial^2 \phi}{\partial X^2} + \frac{\partial^2 \phi}{\partial Y^2} \right) + \frac{\text{N}_T}{\text{N}_B} \left(\frac{\partial^2 \theta}{\partial X^2} + \frac{\partial^2 \theta}{\partial Y^2} \right) \right] \quad (11)$$

The dimensionless stream function ψ is used to represent the streamlines of a fluid along which this function is constant. It can be calculated by:

$$V = -\frac{\partial \psi}{\partial V} \text{ and } U = \frac{\partial \psi}{\partial Y} \quad (12)$$

The solution of these last two equations amounts to the solution of the Poisson equation obtained by deriving the two members of each equation respectively with respect to X and Y. This equation is defined by:

$$\frac{\partial^2 \psi}{\partial X^2} + \frac{\partial^2 \psi}{\partial Y^2} = -\frac{\partial V}{\partial X} + \frac{\partial U}{\partial Y} \quad (13)$$

From the equations Eqs. (7)-(11), many dimensionless numbers appear, namely: the Rayleigh number (Ra), the Hartmann number (Ha), the Prandtl number (Pr), the Lewis number (Le), the number of Brownian motion (NB), the number of thermophoresis (NT) and the ratio of mass buoyancy (Nr) defined respectively by:

$$\begin{aligned} \text{Ra} &= \frac{g \beta_f H^3 (T_h - T_c)}{\alpha_f \vartheta_f}, \text{Ha} = B_0 H \sqrt{\frac{\sigma_f}{\rho_f \vartheta_f}}, \text{Pr} = \frac{\vartheta_f}{\alpha_f}, \text{Le} = \frac{k}{\rho C_p D_B}, \\ \text{N}_B &= \frac{\rho_p C_p D_B}{k_f} \varphi_0, \text{N}_T = \frac{\rho_p C_p D_T (T_h - T_c)}{k_f T_c}, \text{N}_r = \frac{(\rho_p - \rho_f) \varphi_0}{\rho_f \beta_f (T_h - T_c) (1 - \varphi_0)} \end{aligned} \quad (14)$$

The electrical conductivity, density, volumetric expansion coefficient, thermal capacity, thermal conductivity coefficient and dynamic viscosity of the nanofluid are respectively calculated under the following relationships using the properties of the nanoparticles and the base fluid:

$$\rho_{\text{nf}} = (1 - \varphi) \rho_f + \varphi \rho_p \quad (15)$$

$$\sigma_{\text{nf}} = (1 - \varphi) \sigma_f + \varphi \sigma_p \quad (16)$$

$$(\rho \beta)_{\text{nf}} = (1 - \varphi) (\rho \beta)_f + \varphi (\rho \beta)_p \quad (17)$$

$$(\rho c_p)_{\text{nf}} = (1 - \varphi) (\rho c_p)_f + \varphi (\rho c_p)_p \quad (18)$$

$$\alpha_{\text{nf}} = \frac{k_{\text{nf}}}{(\rho c_p)_{\text{nf}}} \quad (19)$$

$$\mu_{\text{nf}} = \frac{\mu_f}{(1 - \varphi)^{2.5}} \quad (20)$$

$$\frac{k_{\text{nf}}}{k_f} = \frac{k_p + 2k_f - 2\varphi(k_f - k_p)}{k_p + 2k_f + \varphi(k_f - k_p)} \quad (21)$$

The coefficient of Brownian motion DB and thermophoresis DT are calculated by the following formulas:

$$D_B = \frac{k_B T_c}{3\pi \mu_f d_p}, \text{ and } D_T = 0.26 \frac{k_f}{2k_f + k_p} \frac{\mu_f}{\rho_f} \varphi_0 \quad (22)$$

3.3. Initial boundary conditions

The system of governing differential equations is provided with the following boundary conditions. For convenience, we restrict ourselves to the dimensionless case:

At the initial time $\tau = 0$:

In the integer domain

$$U = V = 0 (\Psi = 0), \theta = 0 \text{ and } \phi = 1 \quad (23)$$

At the initial time $\tau \geq 0$:

Left and right walls $X = 0$ and $X = 1$.

$$U = V = 0 (\Psi = 0), \theta = 0, N_B \frac{\partial \phi}{\partial N} + N_T \frac{\partial \theta}{\partial N} = 0 \quad (24)$$

Lower and upper wall $Y = 0$ and $Y = 1$.

$$U = V = 0 (\Psi = 0), \frac{\partial \phi}{\partial N} = \frac{\partial \theta}{\partial N} = 0 \quad (25)$$

The walls of the tubes

$$U = V = 0 (\Psi = 0), \theta = 1 \text{ and } N_B \frac{\partial \phi}{\partial N} + N_T \frac{\partial \theta}{\partial N} = 0 \quad (26)$$

3.4. Heat transfer rates

For nanofluid, the Nusselt number is numerically calculated at any position (local Nusselt) by the formula:

$$Nu = - \frac{k_{nf}}{k_f} \frac{\partial \theta}{\partial N} \quad (27)$$

The instantaneous average Nusselt number presents the average of the local Nusselt number in the hot surface (hot pipes). It is calculated as follows:

$$\overline{Nu} = \frac{1}{L} \iint_{\text{hot walls}} Nu \, ds \quad (28)$$

In the case of the thermal cooling, since the wall of the four pipes are hot, the instantaneous average Nusselt number is often calculated at these circular walls (side surface of each tube). The cooling rate is calculated for two Nusselt number values, one is initial Nu_i and the other is final Nu_f as follows:

$$\% C = \frac{\overline{Nu}_f - \overline{Nu}_i}{\overline{Nu}_i} \times 100\% \quad (29)$$

4. Computational details

4.1. Convergence mesh

The system of equations Eqs. (7)-(11) with boundary conditions Eqs. (23)-(26) is solved by the predefined finite element method under COMSOL Multiphysics 5.6. The principle of meshing is to partition the geometric model into several triangles, except for the walls of the cavity, where a rectangular grid has been integrated for adapting the flow pattern, see Fig. 4. Moreover, the adopted mesh is refined close to these walls of the studied cavity. The convergence procedure has been done according to the nonlinear Newton solver. The resolution is considered to be valid when the absolute error between the new and the old value of each dependent variable becomes less than 10^{-6} .

4.2. Mesh check refinement

In order to certify the numerical results, the obtained values of certain important global characteristics from the computational code should be independent of the elements that form the grid mesh and should not be modified by changing the number of these elements. Therefore, several meshes have been tested for achieving this aim. Table 2 shows the elements number used in the simulation and the evolution of the Nusselt number (Nu). The mesh test has been performed for the Nusselt number, the average temperature and the average nanoparticles concentration in the case of a zigzagged cavity with an amplitude of 0.03 and zigzag number 10. The nanofluid flowing at a concentration $\phi = 0.03$ at $Ra = 10^5$ and $Ha = 20$. After a several simulations following the mesh shown in Table 2, it has been opted for a mesh corresponding to an elements number equal 27990. Moreover, in this case, the computation time is not too important.

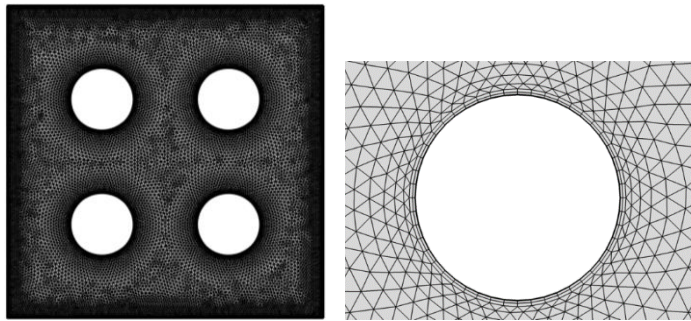


Fig. 4. Mesh of the study domain.

The calculation has been performed by COMSOL Multiphysics 5.6 software, installed on Windows 10. The microcomputer is of type ASUS of 12 GB of RAM with the following processor characteristics: Intel(R) Core(TM) i7-8550U CPU, of basic frequency of 1.80 GHz boosted up to 4 GHz in case of necessity.

Elements number	15666	19226	27990	37900
Time	647 s	647 s	649 s	703 s
Nusselt Number	4.82343	4.82343	4.82343	4.82343
Average temperature	0.64048	0.64048	0.64048	0.64048
Average concentration	0.99985	0.99985	0.99985	0.99985

Table 2. Nusselt number for several numbers of elements.

4.3. Validation

In order to certify the reliability of the numerical simulation and the conformity of the results, we found it necessary to validate the present simulations with previous papers existing in the literature corresponding to the present research focus. Hence, we referred to the paper of Alsarraf et al. 2020. Following the same conditions as in their paper, the thermal profile (Fig. 5.) as well as the variation curve of the average Nusselt number (Fig. 6.) have been showed from the present study compared to the reference (Alsarraf et al. 2020). It seems clear that the present results show good agreement.

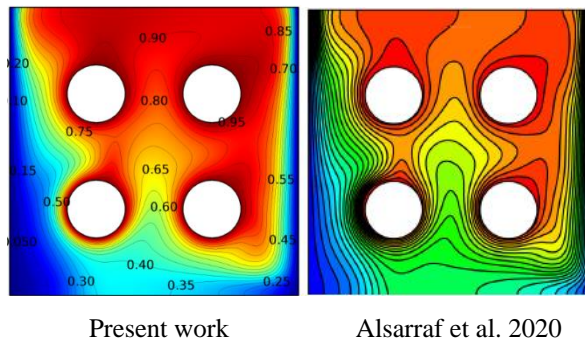


Fig. 5. Comparison of the isotherms of the present study with those of the reference (Alsarraf et al. 2020) for $Ra = 10^6$, $Ha = 50$ and $\phi = 0.03$ and $\gamma = 45^\circ$.

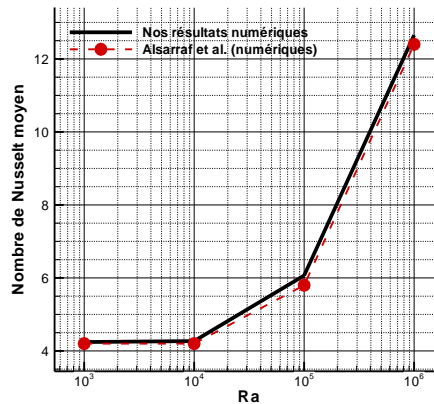


Fig. 6. Comparison of the average Nusselt as a function of Ra of our result with that of the reference (Alsarraf et al. 2020) for $Ha = 50$, $\phi = 0.03$ and $\gamma = 0$.

Ra	Vahl Davis 1983	Alsarraf et al. 2020	Fusegi et al. 1991	Present work
10^3	1.118	1.121	1.141	1.130
10^4	2.243	2.245	2.290	2.320
10^5	4.519	4.519	4.964	4.806
10^6	8.799	8.808	-	9.371
Max error (%)	6.5	6.5	6.3	-

Table 3. Maximum error of the mean Nusselt number compared to the literature (Alsarraf et al. 2020).

In this section, we considered it necessary to establish the rate of deviation of the average Nusselt number calculated from the code used from the well-known reference paper in the field, we are talking here about the Vahl Devis (1983) model. Comparing the maximum relative computational error of our numerical results with those mentioned in Table 2, we observe that it does not exceed 7%. This presents an excellent deviation rate for a numerical calculation performed with such a calculation station. Thus, we see that our results are reliable, stable and consistent, which leads to a good way to introduce any new contribution.

5. Results and discussion

The numerical results are classified for the case of a standard geometry and then for a proposed configuration as a contribution (zigzagged fins). For the nanofluid alumina-water, the velocity profiles, the stream functions, the temperature and nanoparticles local concentration are presented. Moreover, in order to visualize the heat transfer rate of the heat sink, the average total Nusselt number as function of time as well as the average Nusselt number for each pipe are presented according to different parameters. The numerical simulation is based on highlighting the effect of the Rayleigh number ($Ra = 10^3$ to 10^6), the Hartmann number ($Ha = 0$ to 100), the magnetic field tilt angle ($\gamma = 0^\circ$ to 180°) and the amplitude of the zigzagged walls on the capacity of cooling inside the natural heat sink. It should be noted that, the Prandtl number and the mean concentration of the alumina nanoparticles have respectively been set at $Pr = 6.8$ and $\phi_0 = 0.04$. As for the two-phase flow model, the influence of the diameter of the Alumina nanoparticles has been highlighted on the studied behaviors ($dp = 1$ nm to 10 nm).

5.1. Effect of buoyancy

In the present investigation varying Rayleigh number corresponds to the increase in the four cooling pipes temperature following an important thermal generation from the CPU. It can also correspond to the decrease of the temperature of the surrounding environment, for example: the temperature of the room in which the PC is located (for example in the summer and in the winter).

Fig. 7 shows the distribution of nanoparticles, the temperature, and the stream function within the implemented heat sink for different values of the Rayleigh number. The Hartmann number as well as the magnetic field tilt angle are respectively set at 0 and 45° . From the stream function pattern, the density of the nanofluid flow in the vicinity of the four hot pipes walls decreases with the rise of the Rayleigh number. Indeed, this favors the creation of a buoyancy force that leads to the displacement of the hot fluid towards the top of the cavity where the cold fluid moves downwards. On the other hand, the size of the thermal boundary layer increases with the increase in buoyancy intensity especially in the upper part of the heatsink. From Fig. 7, it can be seen a symmetry of the temperature profile with respect to the horizontal median line for the lowest Rayleigh value ($Ra = 10^3$). This symmetry is lost as the Rayleigh values are increased where the hot thermal profile moves towards the top of the heatsink.

The distribution of nanoparticles for the case of Rayleigh number of 10^3 is more important in the immediate vicinity of the cold walls, i.e. the vertical walls of the dissipater. However, it takes its minimum in the vicinity of the walls of the four hot pipes, particularly at the level of the arcs which are exposed to the vertical walls. Indeed, this phenomenon is due to the migration of the nanoparticles towards the low temperature zones by the effect of the thermophoretic diffusion. Moreover, as the buoyancy intensity increases following an increase of the Rayleigh number up to 10^6 , the concentration of nanoparticles becomes more and more important in the lower part of the dissipater. This is due to the decrease of the temperature of the lower part of the heatsink by the impact of buoyancy and its increase in the upper part.

The flow streamlines corresponding to each thermal profile for the different values of the Rayleigh number show a quasi-similarity with the thermal behavior. Indeed, the hydrodynamic structure strongly affects the thermal profile. Thus, the formation of vortices following an increase in buoyancy between the four pipes is directly responsible for the decrease in temperature in this area. In addition, the maximum stream function increases with the increase of the Rayleigh number which means an increase of the nanofluid flow intensity in the heat sink thus, the favor of the heat transfers free convection mode.

Fig. 8 shows the temporal variation of the average Nusselt number of the four hot pipes for various values of the Rayleigh number. This dimensionless number allows to the evaluation of the efficiency of the heat exchange rate explicitly as a function of the Rayleigh number. Moreover, regardless of the value of the latter number, the Nusselt number decreases over time until reaching a steady value, indicating consequently the completion of the steady state on the one hand and the formation of a steady thermal boundary layer on the other hand. Furthermore, from Fig. 8, it is clear that the dimensionless time $\tau = 0.1$ corresponds accurately to a steady state, however for convenience, we have set the time of stability in the whole investigation at the dimensionless instant $\tau = 1$. The decrease of the Nusselt number as a function of time starts from an infinite value at $\tau = 0$.

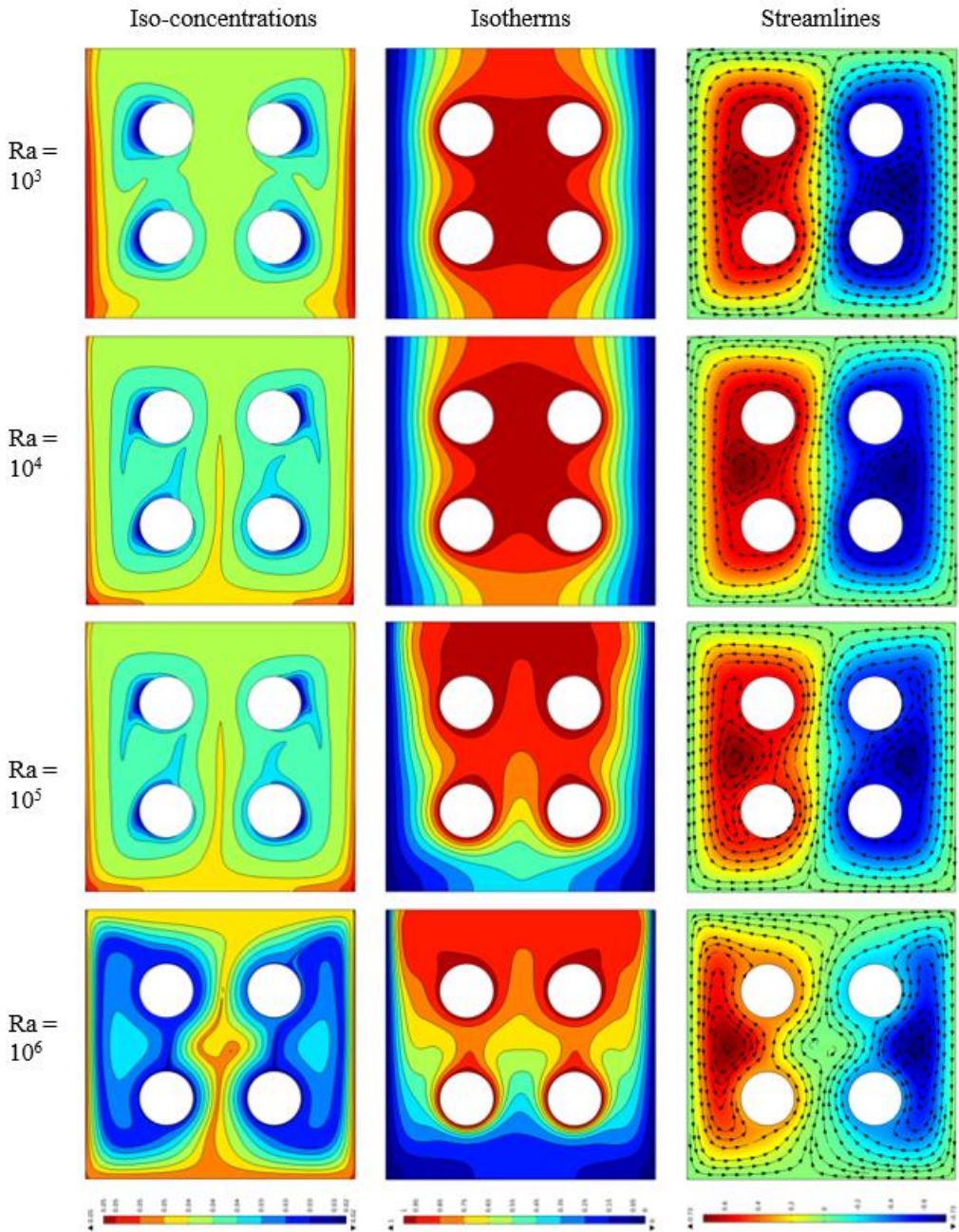


Fig. 7. Iso-concentrations, isotherms and streamlines for different Rayleigh numbers at $Pr = 6.8$, $Ha = 0$ and $\varphi_0 = 0.04$.

This infinite value is obtained according to the initial conditions adopted in the present study with, however, very large thermal gradients at the hot walls of the four pipes. It should be noted that the value of the average Nusselt number in the case of stability is taken as the main value for the thermal efficiency analysis.

To better understand the thermal behavior and the average heat transfer rate obtained at the level of each pipe among the four pipes, it has been found it useful to present the variation of the average Nusselt number corresponding to the steady state for the four pipes in the case of different Rayleigh number values as shown in Fig. 9. From this figure, it has been noted that the most important thermal exchanges occur at the circumferences of the pipes (2) and (3) located in the lower part of the heat sink whatever the value of the Rayleigh number. In fact, due to the decrease in temperature in this area the thermal rate is greater. On the other hand, as the Rayleigh number increases up to the value of 105 the heat transfer rate decreases in the two upper pipes, beyond this value it increases. This is a result of the accumulation of the hot nanofluid in the upper part of the cavity by the influence of buoyancy. However, a significant elevation in terms of buoyancy, favors all the more the natural convective flow stream, and consequently, the stimulation of thermal exchanges. It is worth noting that, although the increase in Rayleigh number in the range of 10^3 to 10^5 favored the heat exchanges near the walls of the two lower pipes, on the other hand, reduced these changes near the upper pipes, the overall heat transfer rate of the four pipes increased. This increase is due to the importance of the improved heat exchanges in the lower pipes compared to those reduced in the upper pipes.

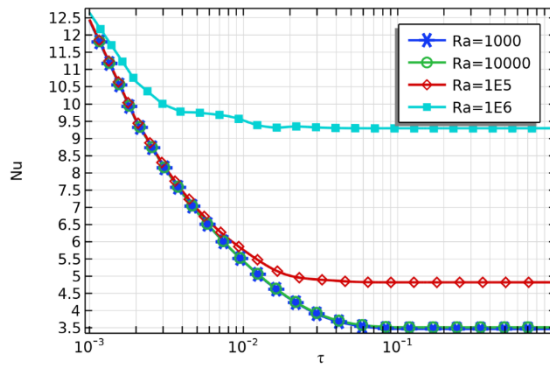


Fig. 8. Average Nusselt number as function of time for different values of Rayleigh number at and $\phi_0 = 0.04$, $Pr = 6.8$ and $Ha = 0$.

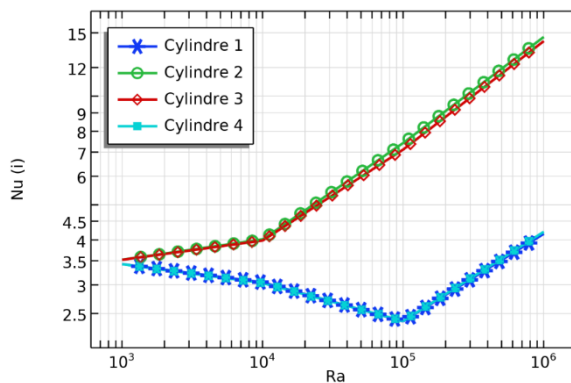


Fig. 9. Average Nusselt number for each pipe for different values of Rayleigh number at $\phi_0 = 0.04$, $Pr = 6.8$ and $Ha = 20$.

5.2. Effect of magnetic field

The non-dimensional analyses provide a generalized qualitative as well as quantitative vision on the behavior of nanofluids electrically conductor subjected a magnetic field. In this case, the Hartmann number is a dimensionless quantity that reflects all the effects of the magnetic flux density on the hydrodynamic, thermal and mass states. Thus, the change of the Hartmann number depends on the variation of the intensity in terms of magnetic field.

Fig. 10 shows the influence of the Hartmann number on the local distribution of nanoparticles, the temperature profile, and the streamlines. It is noted that the Rayleigh number was set to 105 and the magnetic field tilt angle to 45° . From this figure, the increase of the Hartmann number reduces noticeably the flow intensity. Indeed, the maximum stream function is decreased from 5.56 to 1.02. Moreover, the effect of field tilt appears in the case of Hartmann number 80 and 100 where the recirculation loops are tilted by an angle of 45° compared to the case of the absence of the magnetic field ($Ha = 0$). According to the analysis of the temperature contours, it is found that the magnetic field density acts in the opposite direction of buoyancy. In fact, the buoyancy force stimulates the displacement of the hot thermal profile towards the top of the heatsink. However, the magnetic field expressed by the impact of the Lorentz force favors the hot profile to return to the state of the absence of buoyancy and move towards the bottom of the heatsink. Regarding the concentration of Alumina nanoparticles, its distribution is strongly influenced by the direction of the magnetic field (of 45°). With the increase of the Hartmann number, the migration of nanoparticles under the influence of the magnetic field intensifies. Indeed, the accumulation of nanoparticles near the right wall is observed by the effect of the magnetic field.

Fig. 11 shows the time distribution of the average Nusselt number for different values of the Hartmann number. In the steady state, it has been shown that the Nusselt number decreases as the Hartmann number increases. In other words, the addition of a magnetic field tilted by an angle of 45° prevents the rate of heat exchange within the present electronic heatsink, which leads to poor CPU cooling. In the real case, the leakage in terms of magnetic field lines does not have a precise direction, and therefore, further investigation of the effect of the angle of inclination of the magnetic field would have allowed us to identify all the cases that can occur with temperatures and concentrations almost similar to those found in this section.

Fig. 12 shows the variation of the average Nusselt number corresponding to the stability case for different values of the Hartmann number. The analysis of this figure highlights the true interpretation of the decrease in the overall value of the average Nusselt number discussed earlier. In contrast to the case of the influence of buoyancy, it is seen that an increase in the Hartmann number in the range of 0 to 30 causes a decrease in the heat exchange rates in the four hot pipes. However, in the range of Hartmann number from 40 to 100, it is still observed a decrease in heat capacity in the two lower pipes. While it is noticed a relative improvement of this capacity near the two upper pipes. Overall, the high magnetic field strengths in a 45° direction improve the cooling rate in the lower part of such a heatsink. For this purpose, and to prevent the attenuation of the cooling capacity, it has been suggested the installation of the four pipes of the heatsink in its lower part in a way studied on the economic and technological levels.

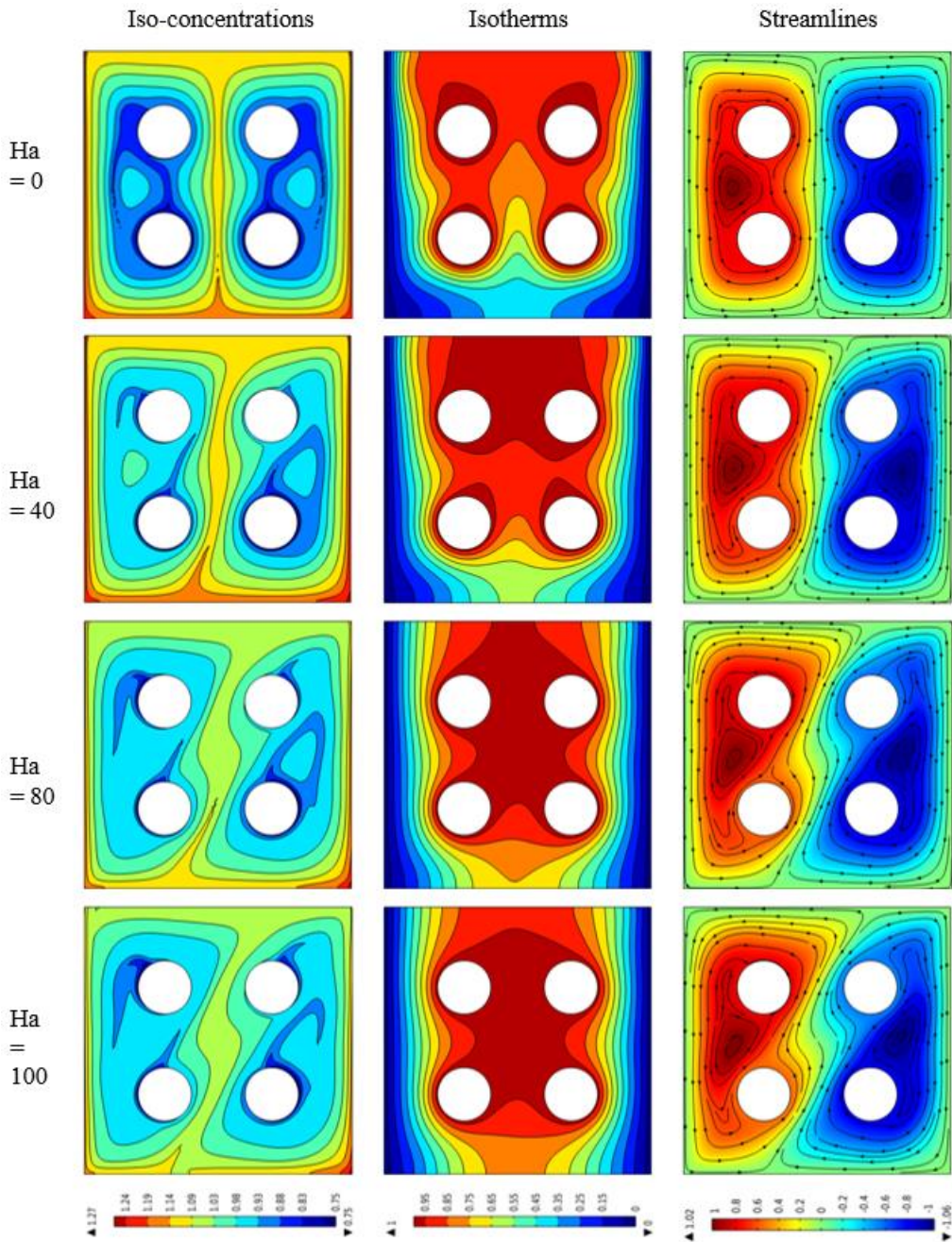


Fig. 10. Iso-concentration, isotherms and Streamlines for different Hartmann numbers and $Pr = 6.8$ and $Ra = 10^5$.

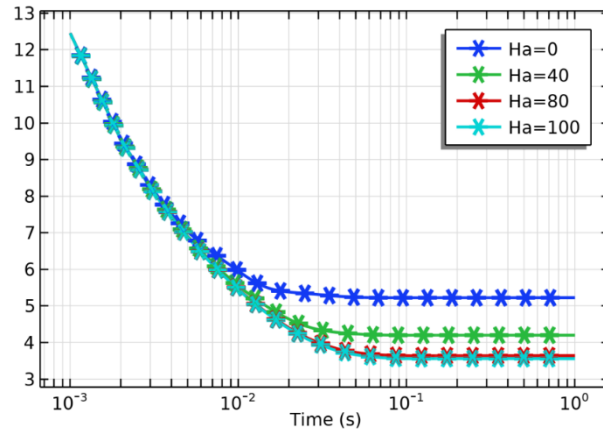


Fig. 11. Average Nusselt number versus time for different values of Hartmann number at $Pr = 6.8$, $\gamma = 45^\circ$ and $Ra = 10^5$.

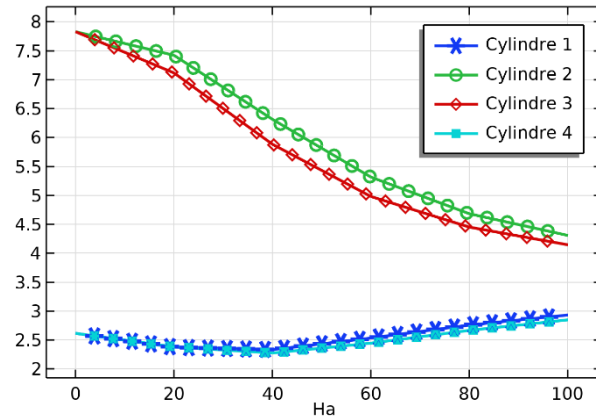


Fig. 12. Average Nusselt number for each cylinder for different values of Hartmann number at $Pr = 6.8$ and $Ra = 10^5$.

5.3. Effect of angle of inclination of the magnetic field

In this part, the influence of the angle of the magnetic field on the capacity of the heat transfer, the structure of the flow and the situation of distribution of the nanoparticles within the heat sink is analyzed. In fact, as we do not know the direction of the magnetic field applied or generated by the electronic components surrounding the heat sink, the extraction of the effect of the inclination angle is presented as a probabilistic investigation on the possibilities of the directions that can appear there.

Fig. 13 shows the nanoparticle distribution, temperature profile as well as the streamlines of the nanofluid flow within the heat sink for different values of the magnetic field tilt angle. Here, the Hartmann number has been fixed at the value of 20. The nanofluid flow within the heat sink is strongly influenced by the increase of the magnetic field inclination angle from a value of 0° corresponding to a Lorentz force applied in the direction of gravity to a value of 90° corresponding to a magnetic force acting in the opposite direction of gravity. In the first case, the flow intensity is entirely weak, where it is noticed the development of several dead recirculation

zones. As the angle of inclination of the magnetic field increases (at 30° and 60°), the intensity of the flow becomes more significant and the low velocity recirculation zones begin to disappear. In this case, the streamlines tilt in accordance with the magnetic field tilt. Then, in the case of an angle of inclination of 90° , the nanofluid flow intensifies, the trajectories return to their vertical state and the dead zones are disappeared. It should be noted that, the maximum value of the stream function increases from a value of 0.58 to 2.08 in the range of variation of the magnetic field angle. Moreover, it appears from this figure that the temperature contours are not totally affected by the increase of the Hartmann number. However, an in-depth analysis of this behavior can be done from the graphs. As for the distribution of the nanoparticle concentration in the heatsink assembly, it is found that the direction of the magnetic field appears as a direct influencing factor. Indeed, the localization of the nanoparticles within the electronic heat sink strongly depends on the direction of the magnetic field lines. Furthermore, in the case of a 90° angle where the Lorentz force is directed in the opposite direction of gravity, the migration of nanoparticles is favored towards the upper part of the heatsink. This migration was present due to the moderation of the electrical conductivity of alumina nanoparticles.

Fig. 14 shows the evolution of the average Nusselt number of the four heatsink pipes as a function of time for different magnetic field tilt angles. It has been shown that the Nusselt number increases relatively by about 8.7% with an increase in the magnetic field tilt angle from 0° to 90° . This increase is mainly due to the influence of the magnetic field tilt angle on the two lower pipes of the heatsink especially pipe (2) which is directly exposed to tilted magnetic field lines, see Fig. 15.

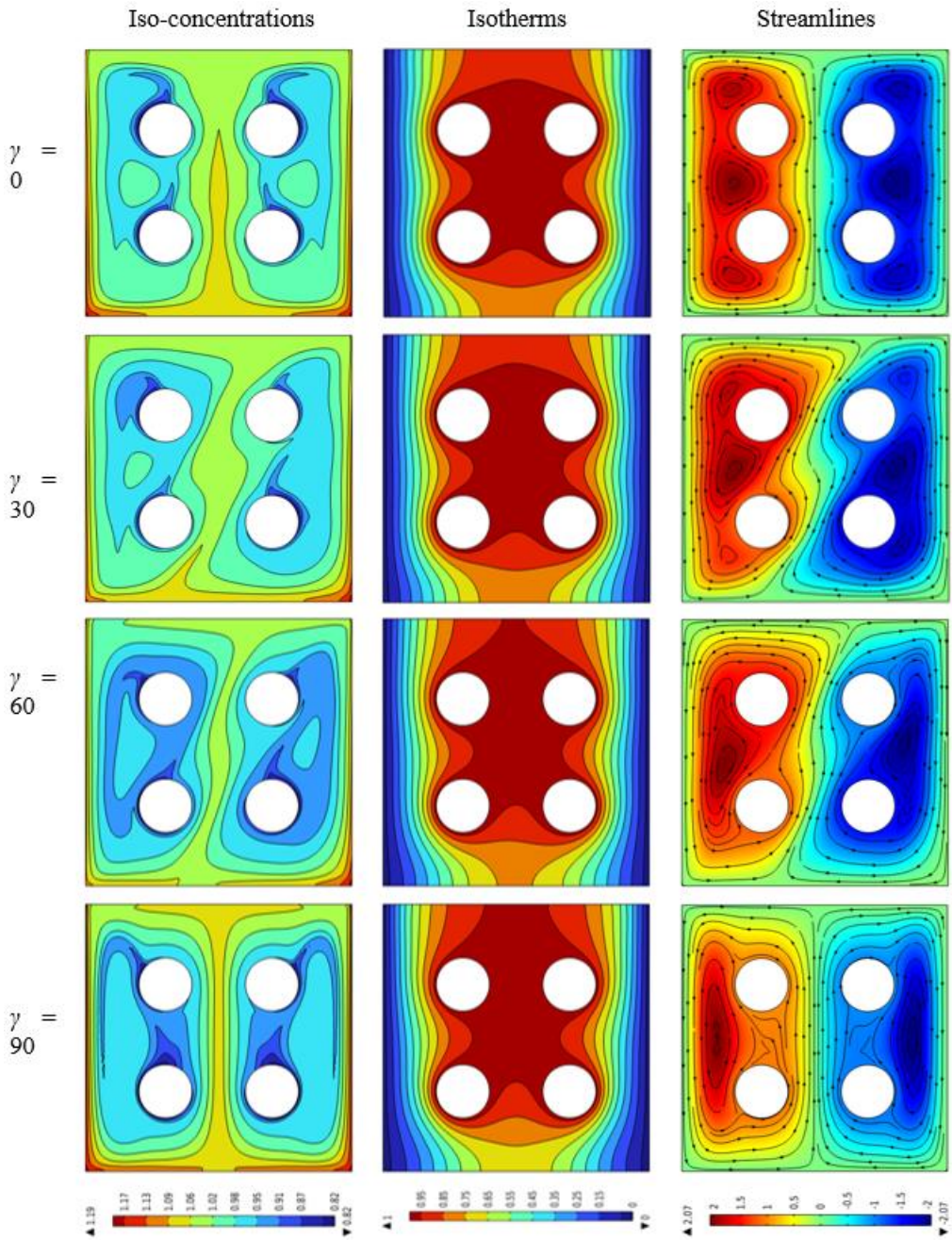


Fig. 13. Iso-concentration, isotherms and Streamlines for different magnetic field tilt angles and $Pr = 6.8$ and $Ha = 20$.

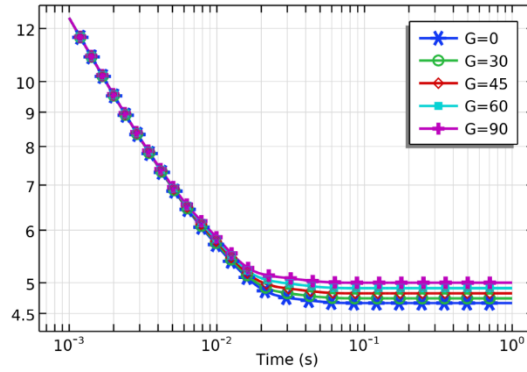


Fig. 14. Average Nusselt number versus time for different magnetic field tilt angles at $Pr = 6.8$ and $Ra = 10^5$.

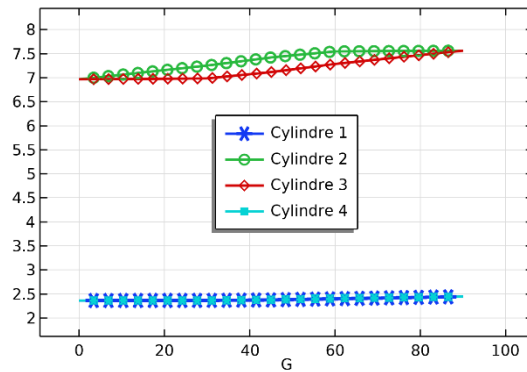


Fig. 15. Average Nusselt number for each cylinder for different magnetic field tilt angles at $Pr = 6.8$ and $Ra = 10^5$.

5.4. Effect of nanoparticles diameter

In nanofluid dynamics, the size of the nanoparticles suspended in the base fluid as well as their shape influence the rate of thermal exchanges while promoting or delaying the intensity of disordered and random movements due to the difference in local concentrations of the nanoparticles that are in contact with the molecules of the base fluid. This is called Brownian motion. In nano-fluidics, Brownian diffusion is an intrinsic characteristic of this type of fluid where the diameter of each nanoparticle can cause relative or even important changes in thermal exchanges. In this section we highlight the impact of the diameter of the alumina nanoparticles on the heat transfer rate within the heat sink for CPU cooling applications. Due to the choice of the Buongiorno mathematical model governing the present studied phenomenon we have limited ourselves to the case of diameters less than 10 nm.

Fig. 16 shows the distribution of nanoparticles concentration, temperature contours as well as flow stream functions for different diameters of alumina nanoparticles. The global analysis of this figure shows that the diameter of the nanoparticles has no significant influence on the thermal and hydrodynamic behavior. Indeed, we do not record any change in terms of isotherms and stream function. On the other hand, the disposition or the migration rate of the nanoparticles is strongly influenced by increasing the diameter of the alumina nanoparticles. Effectively, the nanoparticles concentration increases in the lower part of the electronic heat sink and decreases

in its upper part. The increase in the diameter of the nanoparticles leads to an increase in its mass, and consequently, the migration rate of the nanoparticles under the gravitational effect becomes more significant. In the latter case, the intensity of collisions between water molecules and alumina nanoparticles decreases significantly due to the agglomeration and sedimentation of these nanoparticles at the bottom of the heat sink. However, this phenomenon of sedimentation and agglomeration did not lead to any visible impact on the thermal and hydrodynamic structures.

The analysis of Fig. 17 illustrating the variation of the average Nusselt number of the four pipes over time as well as its average value for each pipe as shown in Fig. 18 allowed us to confirm all the observations made during the analysis of Fig. 15. Indeed, the increase in the diameter of the nanoparticles has no influence on the rate of heat exchange within our electronic heat sink. However, a zoom in in a certain moment allowed us to observe that the rate of heat exchange tends to increase with the increase of the diameter of the alumina nanoparticles. This tendency of increase of the average Nusselt number is due to the tendency of increase of the thermal conductivity of the nanofluid on one hand, and to the decrease of the coefficient of the Brownian diffusion on the other hand.

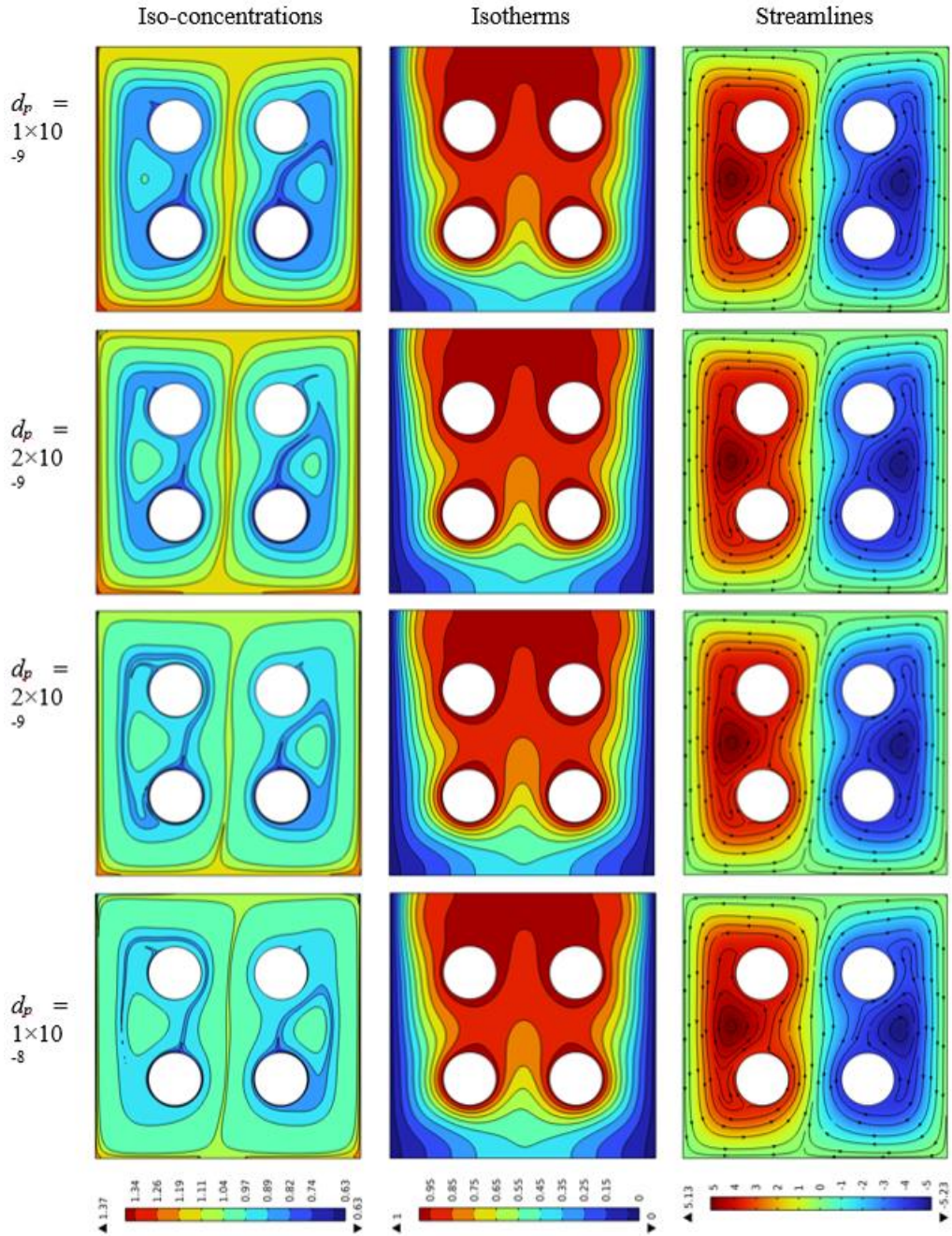


Fig. 16. Iso-concentrations, isotherms and Streamlines for different diameters of nanoparticles at $Pr = 6.8$ and $Ha = 20$.

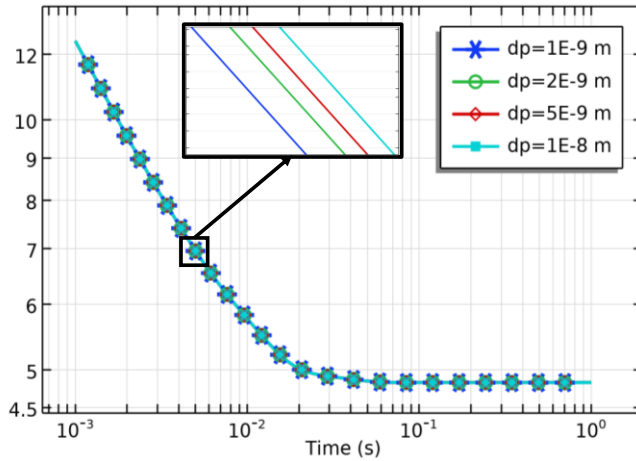


Fig. 17. Average Nusselt number versus time for different diameters of nanoparticles at $Pr = 6.8$ and $Ra = 10^5$.

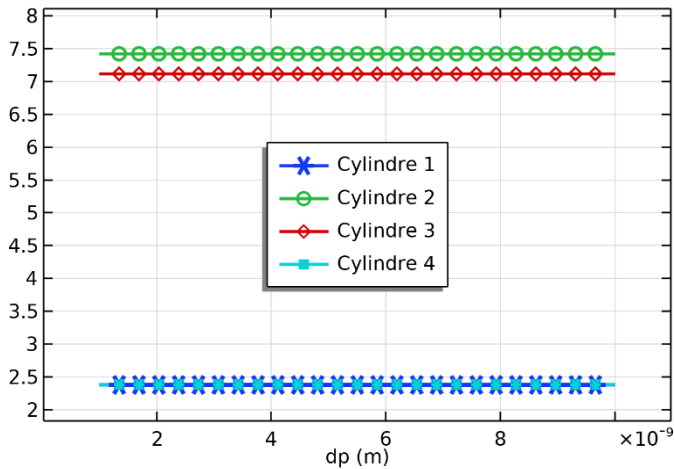


Fig. 18. Average Nusselt number for each cylinder for different diameters of nanoparticles at $Pr = 6.8$ and $Ra = 10^5$.

5.5. Influences of zigzagged walls

Fig. 19 shows the nanoparticle concentration distribution, temperature contours as well as the streamlines for different amplitudes of the zigzagged walls namely the values: 0 (no zigzag), 0.01, 0.03 and 0.05. From the streamlines, it is noted that with the increase of the amplitude of the zigzags the maximum value of the stream function decreases from 3.59 for the case of the standard heat sink to the value of 2.55 for the case of the zigzagged heat sink having an amplitude of 0.05. In addition, it is also noted the formation of dead recirculation zones at the level of the zigzagged cellars, especially those with the largest amplitudes and more particularly in the lower part of the electronic heatsink. In fact, the formation of dead zones leads to a significant reduction in terms of flow velocities, and consequently, a reduction in terms of hydrodynamic intensity. As for the structure of the isotherms, the cold thermal profile intensifies near the zigzagged walls by virtue of the extension of the surface in contact with the ambient air. In this case, the heat transfer

by conduction is favored in this zigzagged region (results of the formation of dead zones). The isotherm shapes remain globally identical far from the zigzagged walls whatever the zigzagging amplitude is. Thus, a further analysis from the graphs will allow us to better visualize the impact of zigzags on the thermal profile.

The distribution of alumina nanoparticles within the studied heat sink is strongly influenced by the new proposed shape. Indeed, from the concentration contours, it is observed an important intensification in terms of nanoparticles migration towards the cellars included between the zigzags of the cold walls by comparing with their accumulation in the lower part of the standard heat sink. Effectively, the enlargement of the low temperature zones leads to the emergence of a considerable thermal gradient. This gradient favors the migration of the nanoparticles towards the low temperature zones under the effect of thermophoretic diffusion. It should also be noted that the development of dead zones between the zigzags presents another factor leading to the agglomeration of nanoparticles exceptionally in this kind of regions.

Fig. 20 shows the distribution of the average Nusselt number as a function of time for different amplitudes of the zigzagged walls. It is observed that despite the reduction in the intensity of the hydrodynamic profile, the average Nusselt number increases as the amplitude increases. Indeed, the rate of heat exchange increases due to the tendency to the solidification state of the dead zones especially with the agglomeration of nanoparticles in this cold region. This is the impact of the high thermal conductivity in this area. Therefore, we took advantage of the thermophoretic migration to improve the heat transfer.

Fig. 21 shows the evolution of the average Nusselt number for each hot pipe as a function of the amplitude of the zigzagged cold walls. We notice that the rate of heat exchange for the two upper pipes is improved as a function of the zigzagging amplitudes, while, we recorded a near reduction in terms of these exchanges at the lower pipes with however an improvement in the overall context. To better understand this, we proceeded to plot Nusselt number graphs for a significant number of the amplitudes, as shown in Fig. 22. Based on the findings from this figure, the use of zigzags as a means of improving heat exchange rates is not always reliable. Certainly, having refined the step change in zigzag amplitude, we found that heat exchange in this case tends to increase with amplitudes beyond 0.016. On the other hand, these exchanges tend to improve with amplitudes that lead to Nusselt numbers exceeding the value obtained in the standard case that is a zigzag with an amplitude of at least 0.028. If this is not the case, the use of the standard configuration is more useful. It should be noted that the rate of cooling improvement with zigzagged walls of 0.05 amplitude compared to the standard case reaches 4%.

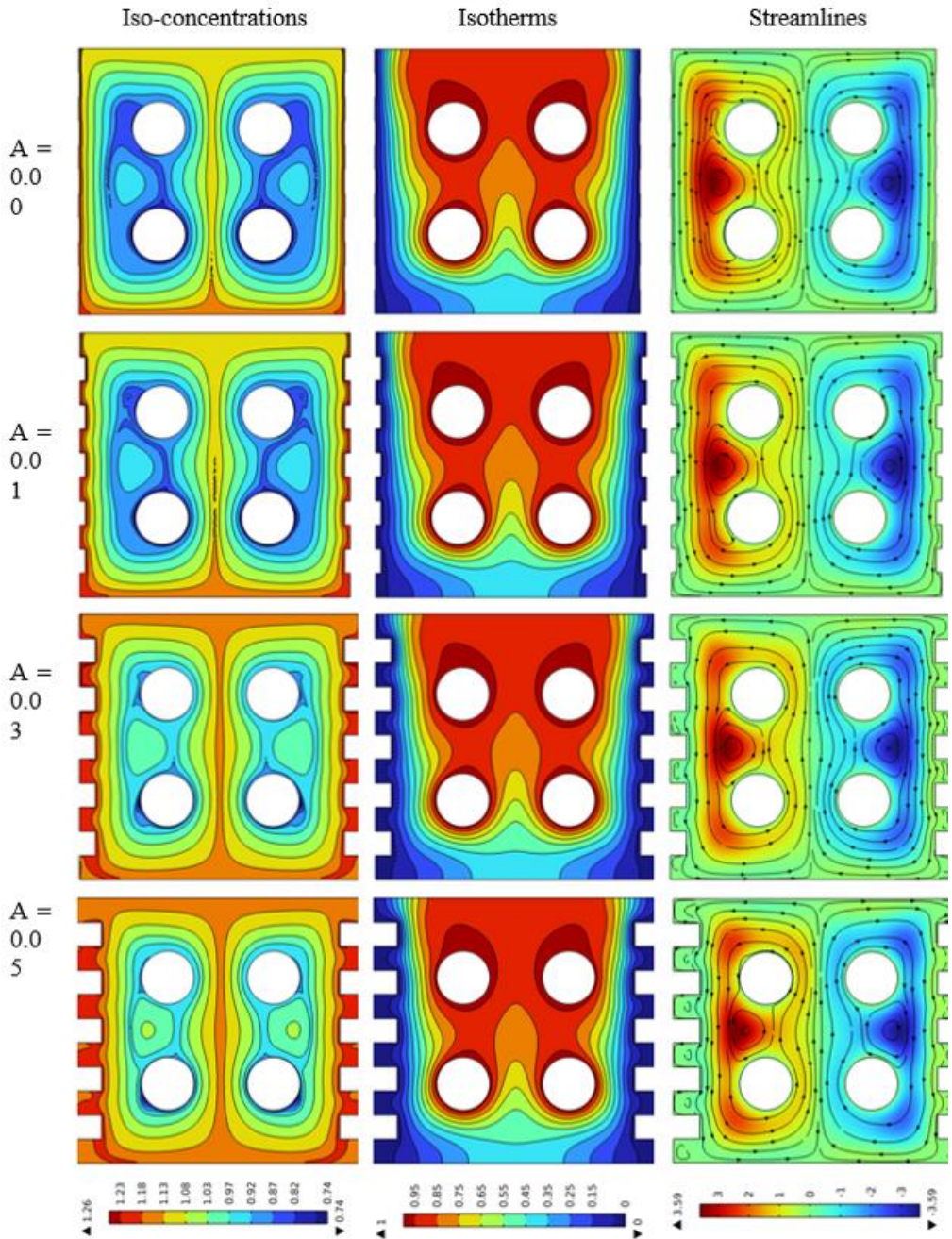


Fig. 19. Iso-concentrations, isotherms and Streamlines for different diameters of nanoparticles at $Pr = 6.8$ and $Ha = 20$.

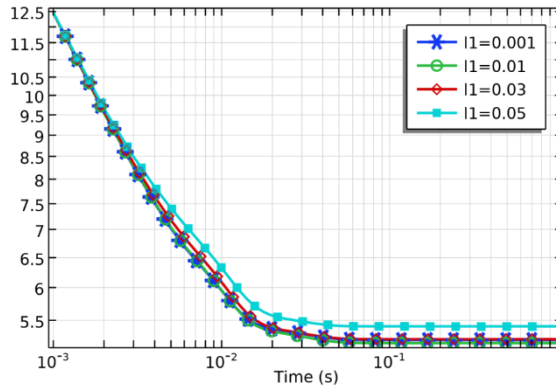


Fig. 20. Average Nusselt number versus time for different zigzag amplitudes at $Pr = 6.8$ and $Ra = 10^5$.

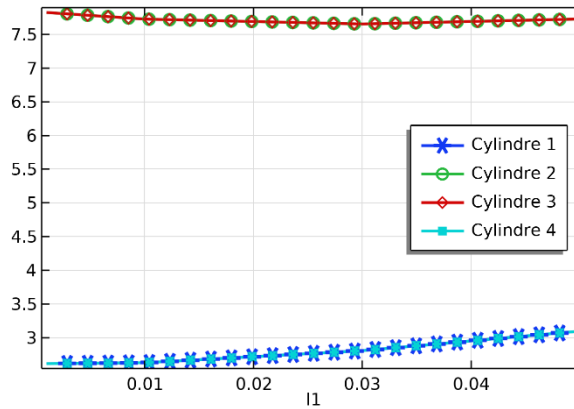


Fig. 21. Average Nusselt number for each cylinder for different zigzag amplitudes at $Pr = 6.8$ and $Ra = 10^5$.

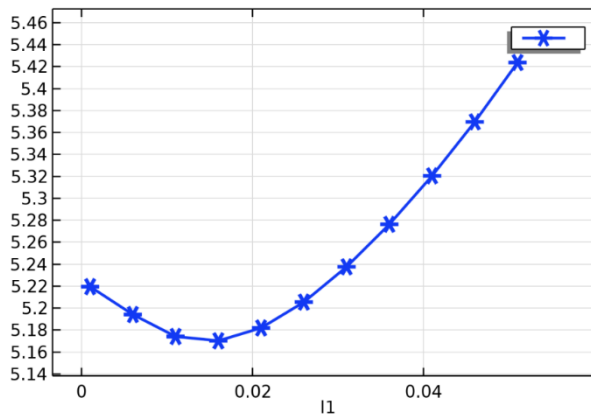


Fig. 22. Average Nusselt number at the stability time for different zigzag amplitudes at $Pr = 6.8$ and $Ra = 10^5$.

6. Conclusions

In this paper, we have presented the results of the numerical simulation of the two-phase Buongiorno flow of a nanofluid within an electronic heatsink designed for CPU cooling. The aim was to examine the influence of some global and geometrical parameters on the improvement of the cooling capacity, namely the effects of: buoyancy, magnetic field and its inclination, volume fraction of alumina nanoparticles and their diameter. As for the geometrical parameters, we proposed a new zigzag shape of the heatsink with different amplitudes. The main points that we can highlight from our investigation are the following:

- The increase of the Rayleigh number favors the rate of thermal exchanges leading to the cooling of the processor. It corresponds to the increase of the thermal generation of the processor or the decrease of the temperature of the surrounding environment.
- The cooling rate of the heatsink decreases in the case of application of a uniform magnetic field, however the inclination of this field has a positive influence on this rate. Indeed, we recorded an improvement rate of 8.7% with a magnetic field inclination of 90°.
- The diameter of the alumina nanoparticles does not affect the cooling rate within our heat sink, however, it favors the migration of nanoparticles to the low areas where the nanoparticles are agglomerated. Thus, the intensity of Brownian motion decreases.
- The new design of the zigzag heatsink that we proposed in our research is suitable with a state of cooling enhancement whose rate is about 4% in the case of a configuration with an amplitude of 0.05 compared to the standard configuration. We have further suggested such a design with amplitudes that exceed 0.028 for which an improvement in terms of heat exchange is assured.
- The new design of the heat sink favors the migration of alumina nanoparticles to the cellars between the zigzags due to thermophoretic diffusion. Moreover, in these zones, we noted a formation of dead zones leading to the stagnation of the nano-fluidic flow between the zigzags.

References

- Aissa A, Al-Khaleel M, Mourad A, Laidoudi H, Driss Z, Younis O, Guedri K, Marzouki R (2022a), Natural convection within inversed T-shaped enclosure filled by nano-enhanced phase change material: Numerical investigation. *Nanomaterials*, 12, 2917.
- Aissa A, Younis O, Al-Khaleel M, Laidoudi H, Akkurt N, Guedri K, Marzouki R, (2022b). 2D MHD mixed convection in a zigzag trapezoidal thermal energy storage system using NEPCM. *Nanomaterials*, 12, 3270.
- Aliouane I, Kaid N, Ameer H, Laidoudi H (2021). Investigation of the flow and thermal fields in square enclosures: Rayleigh-Bénard's instabilities of nanofluids, *Thermal Science and Engineering Progress*, 25, 100959.
- Alsarraf J, Shahsavari A, Khaki M, Ranjbarzadeh R, Karimipour A, Afrand M (2020). Numerical investigation on the effect of four constant temperature pipes on natural cooling of electronic heat sink by nanofluids: A multifunctional optimization, *Advanced Powder Technology*, 31, 416-432.
- Basu S, Jordan E H, Cetegen B M (2008). Fluid mechanics and heat transfer of liquid precursor droplets injected into high-temperature plasmas, *Journal of Thermal Spray Technology volume*, 17, 60–72.

- Chatterjee D, Halder P (2014). MHD mixed convective transport in square enclosure with two rotating circular cylinders. *Numerical Heat Transfer, Part A*, 65, 802–824.
- Chatterjee D, Halder P (2016). Magnetoconvective transport in a lid-driven square enclosure with two rotating circular cylinders. *Heat Transfer Engineering*, 37, 198–209.
- Darzi AAR, Eisapour A H, Abazarian A, Hosseinnejad F, Afrouzi H H (2017). Mixed Convection Heat Transfer Analysis in an Enclosure with Two Hot Cylinders: A Lattice Boltzmann Approach, *Heat Transfer*, 2017, 46, 218-236.
- De Vahl Davis G (1983). Natural convection of air in a square cavity: a bench mark numerical solution, *Int. J. Numerical Methods Fluids*, 3, 249.
- El-Shorbagy MA, Eslami F, Ibrahim M, Barnoon P, Xia WF, Toghraie D (2021). Numerical investigation of mixed convection of nanofluid flow in a trapezoidal channel with different aspect ratios in the presence of porous medium, *Case Studies in Thermal Engineering*, 25, 100977.
- Farahani SD, Sheikhi R, Kisomi MS (2022). Natural convection heat transfer in the annular space by using novel fins and water droplets injection, *Brazilian Journal of Chemical Engineering volume*, 39, 441–454.
- Fusegi T, Hyun JM, Kuwahara K, Farouk B (1991). A numerical study of three-dimensional natural convection in a differentially heated cubical enclosure, *Int. J. Heat Mass Transf.*, 34, 1543–1557.
- Garoosi F, Garoosi S, Hooman K (2014). Numerical simulation of natural convection and mixed convection of the nanofluid in a square cavity using Buongiorno model, *Powder Technology*, 268, 279-292.
- Ghasemi K, Siavashi M (2020). Three-dimensional analysis of magnetohydrodynamic transverse mixed convection of nanofluid inside a lid-driven enclosure using MRT-LBM, *International Journal of Mechanical Sciences*, 165, 105199.
- Guendouci I, Laidoudi H, Bouzit M (2021). The effect of fin length on free convection heat transfer in annular space of concentric arrangement using shear-thinning fluids as a thermal medium, *Defect and Diffusion Forum*, 409, 194-204.
- Hassen W, Borjini MN, Traore P, Ben Aissia H (2013). Electroconvection between coaxial cylinders of arbitrary ratio subjected to strong unipolar injection, *Journal of Electrostatics*, 71, 882-89.
- Ibrahim H, Sazali N, Shah ASM, Abdul Karim MS, Aziz F, Salleh WNW (2019). A Review on factors affecting heat transfer efficiency of nanofluids for application in plate heat exchanger, *Journal of Advanced Research in Fluid Mechanics and Thermal Sciences*, 60, 144-154.
- Karimi F, Xu H, Wang Z, Yang M, Zhang Y (2016). Numerical simulation of steady mixed convection around two heated circular cylinders in a square enclosure. *Heat Transfer Engineering*, 37, 64–75.
- Laidoudi H, Abderrahmane A, Saeed AM, Guedri K, Younis O, Marzouki R, Dong Chung J, Ali Shah N (2022a). Lid-driven chamber with 3D elliptical obstacle under the impacts of the nano-properties of the fluid, Lorentz force, thermal buoyancy, and space porosity, *Nanomaterials*, 12, 2373.
- Laidoudi H, Ameer H (2020a). Investigation of the mixed convection of power-law fluids between two horizontal concentric cylinders: Effect of various operating conditions, *Thermal Science and Engineering Progress*, 20, 100731.
- Laidoudi H, Ameer H (2021a). Natural convection between hot and cold cylinders in enclosed space filled with copper-water nanofluid. *Journal of Thermal Engineering*, 8, 606-618.
- Laidoudi H, Ameer H (2022b). Complex fluid flow in annular space under the effects of mixed convection and rotating wall of the outer enclosure, *Heat Transfer*, 51, 3741-3767.
- Laidoudi H, Ameer H, Sahebi SAR, Hoseinzadeh S (2022c). Thermal analysis of steady simulation of free convection from concentric elliptical annuli of a horizontal arrangement, *Arabian Journal for Science and Engineering*, 47, 15647–15660.

- Laidoudi H, Bouzit M (2017). Mixed convection heat transfer from confined tandem circular cylinders in cross-flow at low Reynolds number, *Mechanics*, 23, 522-527.
- Laidoudi H, Helmaoui M (2020b). Enhancement of natural convection heat transfer in concentric annular space using inclined elliptical cylinder, *Journal of Naval Architecture and Marine Engineering*, 17, 89-99.
- Laidoudi H, Helmaoui M, Bouzit M, Ghenaïm A (2021b). Natural-convection of Newtonian fluids between two concentric cylinders of a special cross-sectional form, *Thermal Science*, 25, 3701-3714.
- Laidoudi H, Makinde OD (2021c). Computational study of thermal buoyancy from two confined cylinders within a square enclosure with single inlet and outlet ports, *Heat Transfer*, 2021, 50, 1335-1350.
- Maneengam A, Laidoudi H, Aissa A, Rasool G, Guedri K, Weera W, Younis O, Bouallegue B, Entropy Generation in 2D lid-driven porous container with the presence of obstacles of different shapes and under the influences of buoyancy and Lorentz forces, *Nanomaterials*, 2022, 12, 2206.
- Matin M H, Khan W A (2013). Laminar natural convection of non-Newtonian power-law fluids between concentric circular cylinders, *International Communications in Heat and Mass Transfer*, 43, 112-121.
- Mishra L, Baranwal A K, Chhabra RP (2017). Laminar forced convection in power-law fluids from two heated cylinders in a square duct, *International Journal of Heat and Mass Transfer*, 113, 589-612.
- Mokeddem M, Laidoudi H, Makinde OD, Bouzit M (2019). 3D Simulation of incompressible poiseuille flow through 180 curved duct of square cross-section under effect of thermal buoyancy, *Periodica Polytechnica Mechanical Engineering*, 63, 257-269.
- Mostafa M (2011). Mixed convection inside nanofluid filled rectangular enclosures with moving bottom wall, *Thermal Science*, 15, 889-903.
- Mourad A, Aissa A, Mebarek-Oudina F, Al-Kouz W, Sahnoun M (2021). Natural convection of nanoliquid from elliptic cylinder in wavy enclosure under the effect of uniform magnetic field: Numerical investigation, *The European Physical Journal Plus*, 136, 1-18.
- Park YG, Yoon H S, Ha MY (2012). Natural convection in square enclosure with hot and cold cylinders at different vertical locations. *International Journal of Heat and Mass Transfer*, 55, 7911-7925.
- Ramla M, Laidoudi H, Bouzit M (2022). Behaviour of a non-newtonian fluid in a helical tube under the influence of thermal buoyancy, *acta mechanica et automatic*, 16, 111-118.
- Rashidi S, Tamayol A, Sadegh M, Valipour, Shokri N (2013). Fluid flow and forced convection heat transfer around a solid cylinder wrapped with a porous ring, *International Journal of Heat and Mass Transfer*, 63, 91-100.
- Rejeb S, Hassen W, Kolsi L, Estellé P (2022). Heat transfer by oil natural convection in an annular space under combined effects of carbon nanotubes and electric field, *International Communications in Heat and Mass Transfer*, 138, 106345.
- Selimefendigil F, Öztöp H F (2015). Influence of inclination angle of magnetic field on mixed convection of nanofluid flow over a backward facing step and entropy generation, *Advanced Powder Technology*, 26, 1663-1675.
- Selimefendigil F, Öztöp H F (2018). Mixed convection of nanofluids in a three dimensional cavity with two adiabatic inner rotating cylinders, *International Journal of Heat and Mass Transfer*, 117, 331-343.
- Selimefendigil F, Öztöp H F (2020). Combined effects of double rotating cones and magnetic field on the mixed convection of nanofluid in a porous 3D U-bend, *International Communications in Heat and Mass Transfer*, 116, 104703.

- Sheikholeslami M, Ellahi R (2015). Three dimensional mesoscopic simulation of magnetic field effect on natural convection of nanofluid, *International Journal of Heat and Mass Transfer*, 89, 799-808.
- Spizzichino M, Sinibaldi G, Romano G P (2020). Experimental investigation on fluid mechanics of micro-channel heat transfer devices, *Experimental Thermal and Fluid Science*, 118, 110141.
- Talkhonchek FK, Xu H, Wang Z, Yang M (2016). Numerical simulation of transient forced convection in a square enclosure containing two heated circular cylinders. *International Journal of Numerical Methods for Heat & Fluid Flow*, 26, 307-327.
- Tayebi T, Chamkha AJ (2021). Analysis of the effects of local thermal non-equilibrium (LTNE) on thermo-natural convection in an elliptical annular space separated by a nanofluid-saturated porous sleeve, *International Communications in Heat and Mass Transfer*, 129, 105725.
- Wu G, Yan Z, Zhuang D, Ding G, Cao F, Meng J (2020). Design method and application effects of embedded-clapboard distributor on refrigerant distribution among multi-tubes of micro-channel heat exchangers, *International Journal of Refrigeration*, 119, 420-433.
- Yang L, Du K, (2020). A comprehensive review on the natural, forced, and mixed convection of non-Newtonian fluids (nanofluids) inside different cavities. *Journal of Thermal Analysis and Calorimetry*, 140, 2033–2054.
- Yigit S, Chakraborty N (2017). Influences of aspect ratio on natural convection of power-law fluids in cylindrical annular space with differentially heated vertical walls, *Thermal Science and Engineering Progress*, 2, 151-164.
- Zeitoun O, Ali M, Nuhait A (2011). Convective heat transfer around a triangular cylinder in an air cross flow, *International Journal of Thermal Sciences*, 50, 1685-1697.